Cross helicity of interplanetary coronal mass ejections at 1 au

Good, S. W.

2022-08

Cross helicity of interplanetary coronal mass ejections at 1 au

S. W. Good [⬛],[1][★] L. M. Hatakka,[1] M. Ala-Lahti,[1,2] J. E. Soljento,[1] A. Osmane[1] and E. K. J. Kilpua[1]

[1]*Department of Physics, University of Helsinki, PO Box 64, FI-00014 Helsinki, Finland*
[2]*Department of Climate and Space Sciences and Engineering, University of Michigan, 2455 Hayward St, Ann Arbor, MI 48109-2143, USA*

ABSTRACT

Interplanetary coronal mass ejections (ICMEs) contain magnetic field and velocity fluctuations across a wide range of scales. These fluctuations may be interpreted as Alfvénic wave packets propagating parallel or antiparallel to the background magnetic field, with the difference in power between counterpropagating fluxes quantified by the cross helicity. We have determined the cross helicity of inertial range fluctuations at 10^{-3} to 10^{-2} Hz in 226 ICME flux ropes and 176 ICME sheaths observed by the *Wind* spacecraft at 1 au during 1995–2015. The flux ropes and sheaths had mean, normalized cross helicities of 0.18 and 0.24, respectively, with positive values here indicating net antisunward fluxes. While still tipped towards the antisunward direction on average, fluxes in ICMEs tend to be more balanced than in the solar wind at 1 au, where the mean cross helicity is larger. Superposed epoch profiles show cross helicity falling sharply in the sheath and reaching a minimum inside the flux rope near the leading edge. More imbalanced, solar wind-like cross helicity was found towards the trailing edge and laterally further from the rope axis. The dependence of cross helicity on flux rope orientation and the presence of an upstream shock are considered. Potential origins of the low cross helicity in ICMEs at 1 au include balanced driving of the closed-loop flux rope at the Sun and ICME–solar wind interactions in interplanetary space. We propose that low cross helicity of fluctuations is added to the standard list of ICME signatures.

Key words: turbulence – Sun: coronal mass ejections (CMEs) – solar wind.

1 INTRODUCTION

Interplanetary coronal mass ejections (ICMEs; e.g. Kilpua, Koskinen & Pulkkinen 2017a) are vast, transient eruptions of plasma and magnetic field from the Sun with properties that are distinct from the solar wind. Signatures of ICMEs may variously include low plasma-β, a smooth rotation of the magnetic field at large scales, and magnetic fluctuations with small amplitudes (e.g. Burlaga 1991; Cane & Richardson 2003). ICMEs with the first two of these signatures are classified as magnetic clouds. ICMEs displaying the second signature may be modelled as flux ropes, with twisted field lines in the ICME volume that wind around a common central axis (e.g. Riley et al. 2004; Al-Haddad et al. 2013). A spacecraft encountering an ICME flux rope will observe a background magnetic field vector that monotonically rotates by up to 180° during the rope passage time. ICMEs are of significant interest as space weather drivers, given that their flux rope structures are a major source of southward magnetic field arriving at Earth (e.g. Wilson 1987; Zhang & Burlaga 1988; Kilpua et al. 2017b). Sheath intervals of compressed solar wind ahead of ICMEs can also be highly geoeffective (e.g. Tsurutani et al. 1988; Lugaz et al. 2016; Kilpua et al. 2017a, 2019).

Like the solar wind, ICME plasma displays broad-band magnetic field and velocity fluctuations with power spectra that take power-law forms (Leamon, Smith & Ness 1998; Liu et al. 2006; Hamilton

et al. 2008; Borovsky, Denton & Smith 2019; Sorriso-Valvo et al. 2021). In the solar wind, most power is contained in Alfvénically polarized fluctuations, with typically a few per cent of total power in other, compressive modes (e.g. Chen 2016). It has long been known that Alfvénic fluctuations with an antisunward sense of propagation predominate over sunward fluctuations in the solar wind (Belcher & Davis 1971), consistent with the fluctuations having mostly a coronal origin. This antisunward predominance is present in fluctuations at low frequencies with an f^{-1} power spectrum and, to a somewhat lesser extent, in turbulent fluctuations at higher frequencies (e.g. Chen et al. 2013). The predominance is also typically greater in fast wind than in slow, and declines with distance from the Sun (e.g. Luttrell & Richter 1987; Marsch & Tu 1990; Bavassano, Pietropaolo & Bruno 2000). The amplitudes of sunward and antisunward fluctuations were found by Borovsky (2012) and Borovsky et al. (2019) to be more equally balanced in ICME plasma at 1 au than in other solar wind types, apart from intervals containing sector reversals in the interplanetary magnetic field. A similar balance was also found by Good et al. (2020) in a magnetic cloud observed at 0.25 au by *Parker Solar Probe* (PSP; Fox et al. 2016). Given that the non-linear interaction of counterpropagating Alfvénic fluctuations is the source of Alfvénic turbulence in the solar wind, the degree of balance or imbalance has a significant effect on the turbulence properties that are observed (e.g. Schekochihin 2020, and references therein).

Imbalance may be quantified in terms of the normalized cross helicity, σ_c, which gives the difference in power between Alfvénic fluctuations propagating parallel and antiparallel to a background magnetic field. We here present analysis of σ_c for a large number

★ E-mail: simon.good@helsinki.fi

of ICME flux ropes and their upstream sheath regions observed by the *Wind* spacecraft at 1 au over a 20-yr period. Fluctuations across a decade of frequencies typically falling within the inertial range of magnetohydrodynamic (MHD) turbulence are investigated, at scales smaller than that of the background flux rope structure. We find that average values of σ_c in the rope and sheath intervals are more balanced (i.e. σ_c is closer to zero) than in the solar wind generally, consistent with previous results. Via superposed epoch analysis, systematic variations in σ_c through the sheath–ICME complex along the heliocentric radial direction have been identified. The dependencies of σ_c on the crossing distance of the spacecraft from the flux rope axis, on the presence or absence of an upstream shock bounding the sheath, and on the flux rope orientation, are also considered.

Cross helicity may be used to define Alfvénicity (e.g. Stansby, Horbury & Matteini 2019). This definition equates high Alfvénicity with the presence of unidirectional Alfvén waves, since such waves have well correlated or anticorrelated magnetic field and velocity fluctuations, and cross helicity is ultimately a measure of this correlation. In this work, cross helicity is interpreted in terms of Alfvénic balance or imbalance, and the normalized residual energy, σ_r, is used to define and measure Alfvénicity. Residual energy, which gives the difference in power between velocity and magnetic field fluctuations, is zero for idealized Alfvén waves but is generally observed to be negative (indicating an excess of magnetic fluctuation energy) in the solar wind inertial range (e.g. Chen et al. 2013). Note that all mentions of cross helicity and residual energy in this work refer to normalized quantities.

In Section 2, the spacecraft data set is described and key parameters are defined. The properties of an example ICME flux rope and sheath interval are described in detail in Section 3.1, followed by analysis of mean properties across all intervals in Section 3.2. In Section 3.3, the superposed epoch analysis is presented, which considers substructuring within the intervals. Possible origins of the low cross helicity in ICMEs and their sheaths are discussed in Section 4.

2 SPACECRAFT DATA

ICME flux ropes catalogued by Nieves-Chinchilla et al. (2018) using *Wind* spacecraft data have been analysed. The catalogue[1] lists 272 intervals with flux rope rotations of the background magnetic field vector that were observed during 1995–2015; intervals in which 5 per cent or more of magnetic field or plasma data were missing have been excluded, leaving 226 intervals included in the present analysis. A total of 176 sheath intervals listed in the catalogue that meet the 5 per cent data gap threshold have also been analysed, of which 97 were associated with shocks.

Magnetic field data from MFI (Lepping et al. 1995) and ion moments from 3DP/PESA-L (Lin et al. 1995) on board *Wind* have been used. Data were typically at 3 s resolution, with linear interpolation applied to close any small data gaps. Measurements of the magnetic field, $\boldsymbol{B}$, proton velocity, $\boldsymbol{v}$, and proton number density, n_p, have been used to determine the Elsasser variables, $z^\pm = \boldsymbol{v} \pm \boldsymbol{b}$, where $\boldsymbol{b} = \boldsymbol{B}/\sqrt{\mu_0 \rho}$ and ρ is the ion mass density. It has been assumed that 4 per cent of solar wind ions are alpha particles and the rest protons by number density such that $\rho = 7 m n_p/6$, where m_p is the unit proton mass. Fluctuations in z^+ and z^- correspond to Alfvénic wave packets propagating antiparallel and parallel to the background magnetic field, respectively.

The trace spectral densities of $\boldsymbol{v}$, $\boldsymbol{b}$ and $z^\pm$, denoted by E_v, E_b, and $E_\pm$, respectively, have been calculated with a Morlet wavelet tech-

nique (Torrence & Compo 1998) and used to obtain the normalized cross helicity,

$$\sigma_c = \frac{E_+ - E_-}{E_+ + E_-} \qquad (1)$$

and normalized residual energy,

$$\sigma_r = \frac{E_v - E_b}{E_v + E_b}. \qquad (2)$$

A similar wavelet method has been applied previously by Chen et al. (2013) to calculate σ_c and σ_r. Values of σ_c and σ_r are limited by definition to the range $[-1, 1]$.

3 ANALYSIS

3.1 An example event

Fig. 1 shows *Wind* observations for one of the ICMEs analysed. The flux rope interval, bounded by vertical grey lines, displays the characteristic rotation of the $\boldsymbol{B}$ vector through a large angle. This rotation is evident in the bottom two panels, which show the latitude angle of $\boldsymbol{B}$ relative to the ecliptic plane, θ, and the anticlockwise angle between the GSE-x (radially sunward) direction and the projection of $\boldsymbol{B}$ on to the ecliptic, ϕ. The θ and ϕ angles are averaged to a resolution of 30 min; we suggest that variations at this time-scale are predominantly due to the global structure of the flux rope. At this scale, $\boldsymbol{B}$ rotated from approximately solar east to north to west through the interval, consistent with the passage of a tube of twisted field lines wound around a central axis with a northward-pointing inclination to the ecliptic. The ordered $\boldsymbol{B}$ rotation, enhanced $|\boldsymbol{B}|$ and low proton plasma-β ($\lesssim$0.1) indicate that the ICME was a magnetic cloud. Horizontal dotted lines in the ϕ panel denote the nominal sector boundaries of the interplanetary magnetic field assuming a Parker spiral angle of 45°, with ϕ values between (outside) the lines indicating field in the away (toward) sector. The sheath interval was bounded by a shock,[2] marked by the vertical gold line, and the leading edge of the flux rope. A second shock was present within the sheath.

Wavelet spectrograms of σ_r and σ_c in the frequency range 3.2×10^{-5} to 10^{-2} Hz are displayed in Fig. 1. Spectrograms of time intervals longer than those shown in Fig. 1 were obtained, such that the intervals which are shown in the figure fall entirely within the cone of influence. Upstream of the shock, slow wind with strongly negative σ_c was present. Since the mean field was mostly in the away sector in this upstream region, negative σ_c (i.e. greater power in z^- than z^+ fluctuations) here indicates the prevalence of fluctuations with an antisunward sense of propagation in the plasma frame. Antisunward fluctuations were likewise prevalent in the faster solar wind trailing the ICME during April 6, where σ_c was strongly positive and the mean field was in the toward sector. In both the upstream and downstream intervals, $|\sigma_r|$ was low (indicative of fairly Alfvénic wind) and almost entirely negative.

The flux rope interval displayed a patchy mix of positive and negative σ_c, with a globally averaged value close to zero. This local patchiness in σ_c is a fundamental feature of balanced turbulence as predicted by models (Perez & Boldyrev 2009). Values of σ_r were lower in the flux rope than in the ambient solar wind, particularly at the lower end of the frequency range. As in the upstream wind, σ_c was globally negative in the sheath, but with significant positive patches that increased the mean value. Globally, there was little difference between σ_r in the sheath and ambient wind.

---

[1]https://wind.nasa.gov/ICMEindex.php
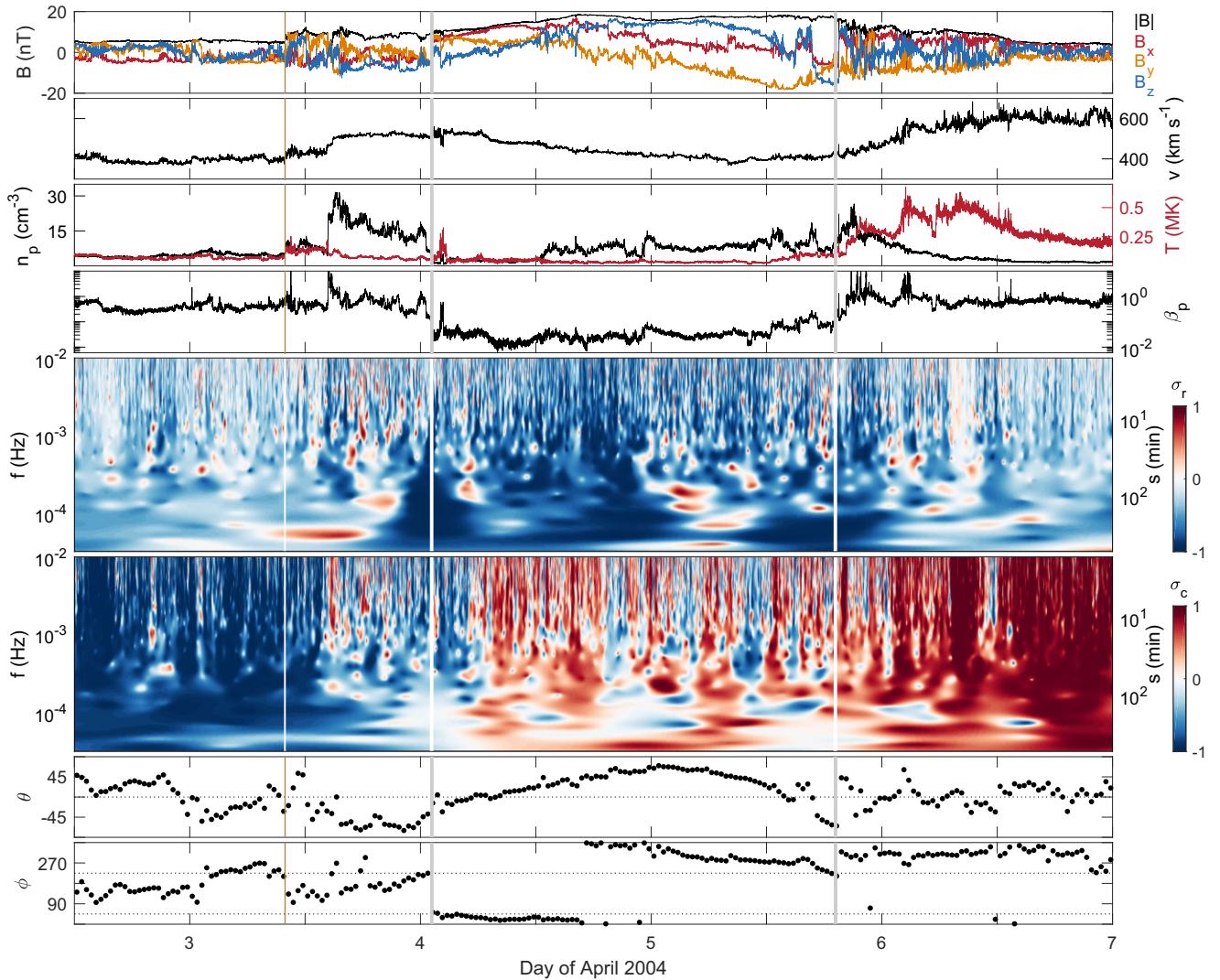
[2]http://www.ipshocks.fi

Figure 1. An example ICME. From top to bottom, the panels show the magnetic field in GSE coordinates; bulk proton speed; proton density and temperature; proton plasma-β; normalized residual energy; normalized cross helicity; and 30-min averages of the magnetic field latitude and longitude angles in GSE coordinates. The ICME boundaries and upstream shock are marked by grey and gold vertical lines, respectively.

In the following, we restrict our analysis to the frequency range 10^{-3} to 10^{-2} Hz (equivalent to wave periods $1.67-16.7$ min). The inertial range of MHD turbulence usually encompasses these frequencies at 1 au (e.g. Kiyani, Osman & Chapman 2015). At much larger scales (e.g. frequencies $\lesssim 10^{-4}$ Hz, periods $\gtrsim 2.8$ h), a significant fraction of fluctuation power in an ICME may be due to the variation of the flux rope B-field. Rather than this background, mean-field structure, we focus on smaller scale fluctuations present within the structure. At 10^{-3} to 10^{-2} Hz, the ICME shown in Fig. 1 had globally averaged $\{\sigma_c, \sigma_r\}$ values of $\{0.10, -0.47\}$ in the flux rope and $\{-0.38, -0.26\}$ in the sheath. The sample points used to determine these averages were equally spaced across the logarithmic frequency range.

3.2 Mean values

Fig. 2 shows the globally averaged values of σ_r versus σ_c at 10^{-3} to 10^{-2} Hz for the 226 flux rope and 176 sheath intervals analysed. Values are constrained by definition to fall within the circle described by $\sigma_r^2 + \sigma_c^2 = 1$. The mean of the globally averaged σ_r values for the flux rope intervals was -0.36, similar to the mean of -0.35 found

for the sheath intervals. None of the flux rope or sheath intervals had a globally positive value of σ_r.

Points in Fig. 2 are colour coded according to the fraction of data in the corresponding interval that was in the away sector, χ. Red ($\chi > 0.5$) and blue ($\chi < 0.5$) points indicate intervals that were primarily in the away and toward sectors, respectively. For the sheath intervals, the sector structure is defined relative to the Parker spiral as described in Section 3.1. For the flux ropes, which do not have a Parker spiral field, we define a sector structure based on the distributions of GSE ϕ angles observed within ICMEs obtained by Borovsky (2010). In fig. 3 of Borovsky (2010), broad peaks at around $120°$ and less distinctly at $300°$ can be seen in the distributions for three different ICME catalogues. These two angles are used as the mid-points of the away and toward sectors for the flux rope intervals (cf. $135°$ and $315°$ for the equivalent Parker spiral sectors).

The anticorrelation of σ_c and χ that can be seen in Fig. 2 is consistent with the prevalence of antisunward fluctuations: when the mean field is in the away (toward) sector, σ_c tends to be negative (positive) and fluctuations in the antisunward z^- (z^+) mode are dominant. A meaningful average value of σ_c across all intervals is obtained by first rectifying the magnetic field, so that positive σ_c
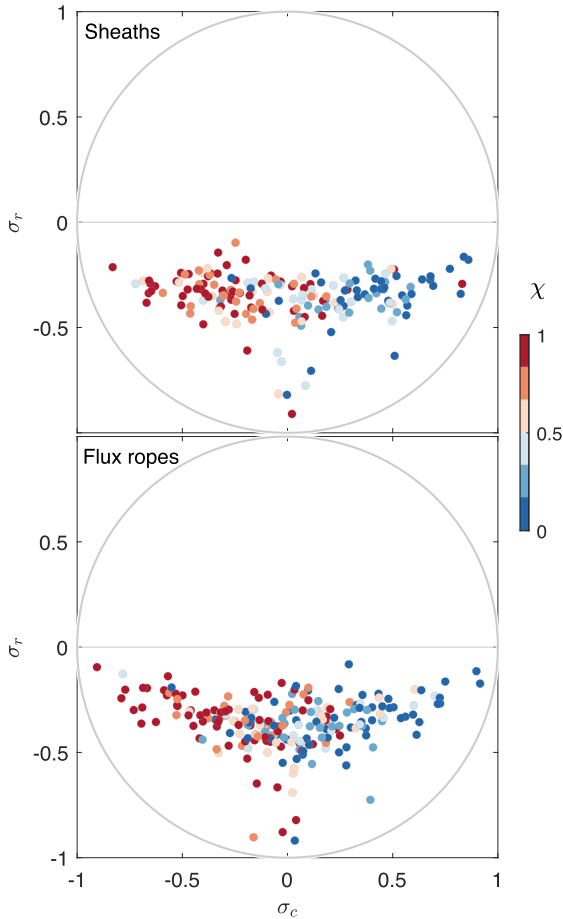
Figure 2. Globally averaged values of σ_r versus σ_c across the upstream sheath regions (top panel) and flux rope intervals (bottom panel). The χ parameter gives the fraction of the interval in the away sector.

is defined as the antisunward flux regardless of the interval sector. This rectification is achieved by reversing the mean field direction for the away sector intervals, equivalent to reversing the sign of σ_c for the points with $\chi > 0.5$ in Fig. 2. The mean value of rectified cross helicity, σ_c^*, was 0.18 for the flux rope intervals and 0.24 for the sheaths, in both cases closer to zero than the average solar wind value of 0.40 found by Chen et al. (2013). In practice, the mean σ_c^* value for the flux ropes is the same for sector boundaries defined relative to the Borovsky distributions and the Parker spiral, although the χ values for some individual intervals are sensitive to the choice of sector boundary definition.

A low average value of $|\sigma_c|$ in a particular interval may arise simply if the interval has a mixed sector structure. When excluding intervals with $1/6 < \chi < 5/6$ in Fig. 2 (i.e. paler-shaded points), which have a more mixed structure, the mean values of σ_c^* become 0.24 for the flux ropes and 0.31 for the sheaths, higher than the all-interval means but still lower than the solar wind average. This suggests that the low cross helicity found in this analysis is only partially due to a mixing of sectors, and that it is a more intrinsic property of the fluctuations.

3.3 Dependence on ICME parameters

ICMEs are often observed by spacecraft as highly structured intervals with systematic variations in properties. Variations may, for example, be seen from the front to the back of an ICME flux rope as it passes

over an observing spacecraft (e.g. Lynch et al. 2003; Masías-Meza et al. 2016; Rodriguez et al. 2016). Properties also vary depending on flux rope orientation, and on which region of the rope's 3D structure that happens to be observed. Sheaths likewise show systematic variations in properties from their leading edges to the interface with the driver material (Kilpua et al. 2019; Salman et al. 2020; Kilpua et al. 2021), and also in the lateral direction (Ala-Lahti et al. 2020). Spatial variations in σ_c^* and $E_\pm^*$ from the front to back of the sheath–flux rope complex, and the dependence of these variations on a range of global ICME parameters, are considered. Here, E_+^* and E_-^* represent power in fluctuations with an antisunward and sunward sense of propagation in the plasma frame, respectively (cf. unrectified $E_\pm$).

Flux rope fitting parameters obtained by Nieves-Chinchilla et al. (2019) have been used to categorize the 226 flux rope intervals. The fits were performed with the circular-cylindrical model derived by Nieves-Chinchilla et al. (2016), which characterizes flux ropes as axially symmetric cylinders of twisted magnetic field. Fitting of the model to the observed $\boldsymbol{B}$ timeseries with a chi-square minimization gives various global parameters of the flux rope; of relevance here are the latitude, θ_0, and longitude, ϕ_0, of the flux rope axis direction in GSE coordinates, the flux rope handedness, H, which may be either left (-1) or right ($+1$) handed, and the impact parameter, $p = |y_0/R|$, which gives the distance of closest approach made by the spacecraft to the flux rope axis, y_0, as a fraction of the rope radius, R.

3.3.1 All-event profiles

Fig. 3 shows superposed epoch profiles of σ_r, σ_c^* and $E_\pm^*$ for the flux ropes and sheaths. These profiles were produced by normalizing the time span of each rope and sheath interval, and then dividing each into 16 and 6 sub-intervals, respectively. The average value of each parameter in each sub-interval was determined from the wavelet spectrograms, then averaged across all events by sub-interval number to give the profiles shown. Sub-intervals in a particular event with 5 per cent or more of data missing were excluded. Rectification to obtain σ_c^* and $E_\pm^*$ was performed with the χ value calculated in each sub-interval, using the method described in Section 3.2. This procedure was applied to the rope and sheath intervals separately. The mean durations of the flux rope and sheath sub-intervals were approximately equal, at 1.5 and 1.6 h, respectively. Single points for intervals spanning 6 h immediately preceding the sheath and following the rope are also shown. The profiles in Fig. 3 represent cuts in the radial heliocentric direction through the sheath–flux rope complex. The leading and trailing edges of each profile have normalized time-scale values of '0' and '1', respectively; the trailing edge of the sheath (at '1' on the sheath profile x-axis) is equivalent to the leading edge of the flux rope (at '0' on the rope profile x-axis).

The σ_r profile displays a sharp drop followed by a plateau at lower values in the sheath, and an uneven rise from the leading to trailing edge of the flux rope. The more Alfvénic σ_r value of the first data point in the sheath profile (-0.31) is attributed to fluctuations generated immediately downstream of shocks: the profile including only sheaths with shocks (not shown) displays this more Alfvénic downstream region, while the equivalent profile for sheaths without shocks is flat throughout, at $\sigma_r \sim -0.36$. The spread in σ_r values across the profile is relatively narrow.

The σ_c^* profile shows, from front to back, a slight decrease from the upstream solar wind in the front half of the sheath, a sharp drop towards the sheath rear, a minimum within the flux rope close to the
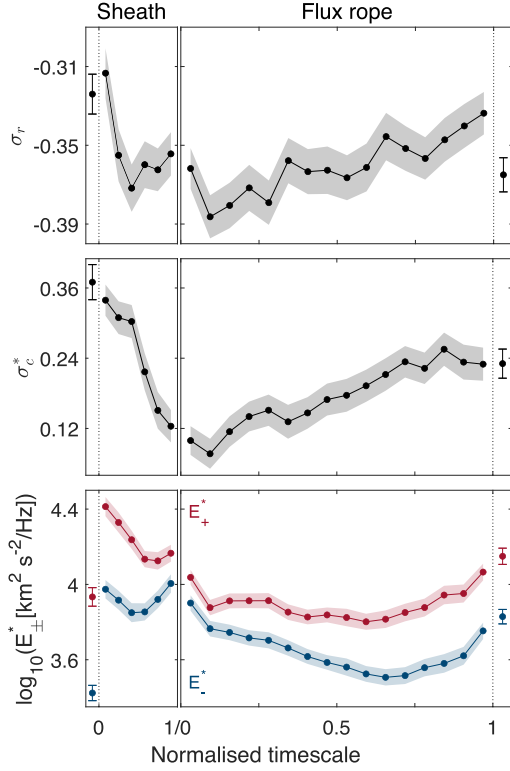
Figure 3. Superposed epoch profiles of σ_r, σ_c^*, and $E_\pm^*$ for sheaths (left-hand panels) and flux ropes (right-hand panels), made by binning all events. Dashed lines indicate the start and end of the ICME profile. Single bins spanning 6 h of solar wind before and after the ICMEs are also shown. Shading and error bars indicate the standard error of values in each bin.

Table 1. Mean interval-averaged values of σ_r and σ_c^* in ICME sheaths and flux ropes. Standard deviations (SD) are also listed.

	Residual energy		Cross helicity	
	σ_r	SD	σ_c^*	SD
Sheaths	-0.35	0.12	0.24	0.30
Flux ropes	-0.36	0.13	0.18	0.29

sheath–flux rope interface, and a gradual rise towards the flux rope trailing edge. The average σ_r and σ_c^* values across the sheath and rope profiles are consistent with the values in Table 1, as expected. While remaining at low values, the average σ_c^* is in all locations positive, indicating that the balance is tipped towards the antisunward direction throughout the ICME.

It is instructive to consider variations in E_+^* and E_-^* individually, recalling that σ_c^* is the normalized difference between these two quantities. The $E_\pm^*$ profiles in Fig. 3 show the typical dominance of E_+^* over E_-^* in the solar wind upstream of the sheath. From upstream wind to sheath, there is a sharp increase in E_+^* and E_-^*, with both then showing a central dip and rise towards the sheath rear. It can be seen that the drop in σ_c^* at the sheath rear is due to a relatively greater enhancement in E_-^* than E_+^*. In the front two-thirds of the flux rope, the flat E_+^* combined with a falling E_-^* causes the rising σ_c^* noted previously. Both E_+^* and E_-^* gradually rise towards the back of the rope.
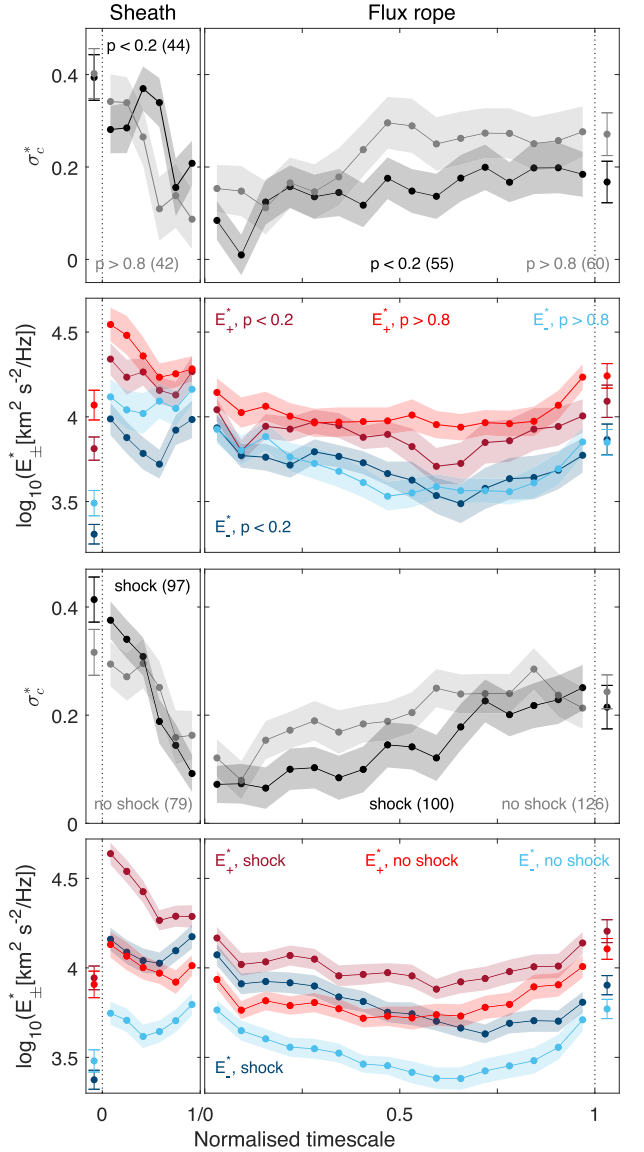

Figure 4. Superposed epoch profiles of σ_c^* and $E_\pm^*$ binned according to high and low impact parameter, p, and to the presence or absence of an upstream shock, in a similar format to Fig. 3. The number of events contributing to each profile is given in parentheses in the σ_c^* panels.

3.3.2 Impact parameter and shocks

The first and second rows in Fig. 4 show profiles separated according to whether the impact parameter through the flux rope was high ($p >$ 0.8) or low ($p < 0.2$). Lower σ_c^* can generally be seen across the rope at low p, when the spacecraft trajectory came closer to the central axis, while higher, more solar wind-like σ_c^* tends to be found at high p, further from the central axis. This σ_c^* versus p trend is primarily due to higher E_+^* at large p within the rope, although the differences in $E_\pm^*$ between high and low p encounters is not large. There are weak signatures of correlated W-shaped profiles in E_+^* and E_-^* across the rope at low p.

The bottom two rows of Fig. 4 display profiles for sheaths and ropes sorted according to whether or not an upstream shock was present. It can be seen that $E_\pm^*$ are significantly higher for the shock-associated profiles, to the extent that E_-^* in the shock-associated profiles is equal to or greater than E_+^* in the non-shock profiles
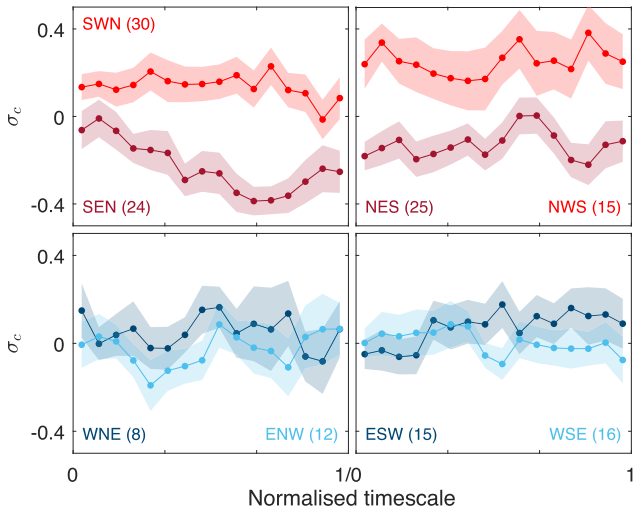
Figure 5. Superposed epoch profiles of σ_c for flux ropes with a low inclination (red lines) and high inclination (blue lines) relative to the ecliptic plane, in a similar format to Figs 3 and 4.

through the sheath and front half of the rope. The resulting differences in σ_c^* are less significant, however, with σ_c^* being somewhat lower in the shock-associated profile through the rope, and about the same in both profiles through the sheath.

3.3.3 Flux rope structure

Fig. 5 shows σ_c profiles for flux ropes sorted into the eight categories devised by Bothmer & Schwenn (1998) and Mulligan, Russell & Luhmann (1998). Each category has a three-letter designation, with the letters giving in sequential order the field polarity observed near the rope leading edge, central axis, and trailing edge. Polarities are given in terms of the solar cardinal directions, where N (north) $\simeq +B_z$, S (south) $\simeq -B_z$, E (east) $\simeq +B_y$ and W (west) $\simeq -B_y$. For example, the rope displayed in Fig. 1 is ENW type, given the approximate rotation from east ($\theta = 0°$, $\phi = 90°$) to north ($\theta = 90°$) to west ($\theta = 0°$, $\theta = 270°$). Four categories are associated with intrinsically left-handed ropes (SEN, NWS, ENW and WSE) and four with right-handed ropes (SWN, NES, WNE and ESW). Flux ropes were sorted into the eight categories using H, θ_0 and ϕ_0 from the Nieves–Chinchilla fits, with axis direction bins centred on each of the four cardinal directions and spanning 90° in latitude and longitude. Ropes with axis directions closer to the $\pm x$ directions, which do not fall into the eight-category classification system described above, are generally more difficult to fit accurately with cylindrical models and have been excluded from the present analysis. Note that we have reverted to using unrectified σ_c in this analysis, so that the mean field direction is inferred from the flux rope structure rather than the sector structuring previously used.

The top panels in Fig. 5 show profiles for ropes at a low inclination to the ecliptic (i.e. with eastward or westward axes), and the bottom panels show profiles for highly inclined ropes (i.e. with northward or southward axes). The profiles are paired in a way that matches south with south and north with north, and juxtaposes east and west. It can be seen that ropes with a westward axis (SWN and NWS) tend to have positive σ_c and ropes with an eastward axis (SEN and NES) have negative σ_c. Given that the profiles show unrectified σ_c values, this trend corresponds to a predominance of eastward-propagating Alfvénic fluctuations in all four low-inclination rope categories.

Considering the sense of solar rotation, the eastward direction will tend to be antisunward at 1 au. However, this assessment is complicated if we envision flux ropes as closed loops with both ends connected to the Sun, i.e. both east and west are ultimately sunward on a closed loop. This issue is discussed further in Section 4.

The four high-inclination profiles are more overlapping than the low-inclination profiles, with σ_c values generally closer to zero. If the same east versus west trend were seen as for the low-inclination ropes, the high-inclination profiles would be bimodal, i.e. W–E ropes would show a positive to negative change in σ_c, and vice versa; using solar wind sector phenomenology, high-inclination ropes are mixed-sector intervals. However, there is little evidence of this bimodality in Fig. 5, with only a very weak signature of it in the profiles shown in the bottom right panel. The relatively low number of events contributing to the high-inclination profiles may not be sufficient for any systematic bimodality to become distinguishable from the random statistical variations between events. There is also likely to be a dependence on the sign and magnitude of y_0/R for the high-inclination ropes, but the low event numbers preclude further investigation in terms of superposed epoch profiles. Alternatively, it may be that the east–west trend in σ_c is only present when the east–west field in question forms part of the rope's axial field (top panels) rather than the rope's outer, poloidal field (bottom panels). The polarity of the axial field appears to dominate the overall σ_c sign across the flux rope. Northward and southward field may be either sunward or antisunward, which may explain why there is no consistent north–south trend in σ_c in any of these averaged profiles.

4 DISCUSSION

4.1 Solar origins

Envisioned as closed loops with both footpoints anchored to the photosphere, ICME flux ropes could in principle carry a relatively balanced population of Alfvénic fluctuations from the corona and across the Alfvén critical point. Such a balanced state would arise if antisunward fluctuations have sufficient time (before the rising loop has crossed the critical point) to propagate up one side of the loop and down the other, where they would become sunward-directed. Mixing of fluctuations propagating in both directions around the loop could thus produce a balanced state right up to the critical point, which then becomes 'frozen-in' and swept out with the supersonic flow at higher altitudes. This contrasts to open solar wind field lines, along which only an antisunward component is carried above the critical point. A number of sources have been suggested for the sunward fluctuations that are observed in the solar wind in interplanetary space, including reflection off the radial gradient in the Alfvén speed (e.g. Chandran et al. 2011), parametric decay (e.g. Bowen et al. 2018) and generation within interaction regions (e.g. Smith et al. 2011). In an ICME flux rope, in contrast, there is the intriguing possibility that the coronal source of antisunward fluctuations is also a source of the sunward fluctuations.

This closed-loop scenario was previously outlined by Good et al. (2020), and, in a similar vein, Borovsky et al. (2019) have discussed how Alfvénic properties of solar wind at 1 au may be partly determined by the degree to which coronal source regions are open or closed. The low cross helicity of fluctuations in ICME flux ropes at 1 au may be a direct remnant of the coronal activity described above, or an indirect signature that develops via a turbulent cascade: balanced, low-frequency driving of the flux rope loop in the corona and beyond would produce balanced turbulence at the higher, inertial range frequencies that we have examined.
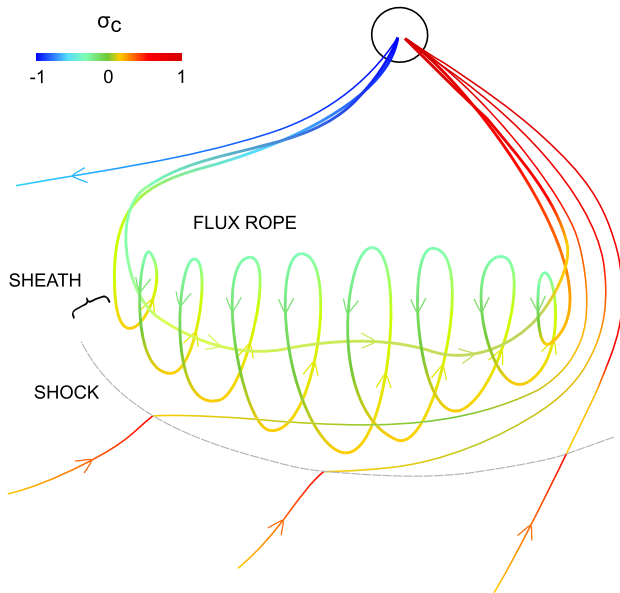
Figure 6. Cross helicity in an ICME with a flux rope, sheath and shock substructure, propagating through the Parker spiral. Solid lines show the mean field, with the cross helicity of Alfvénic fluctuations at smaller scales indicated by the line colour. Blues and reds show regions where fluctuations are propagating parallel and antiparallel to the local field direction, respectively, with green shades indicating a balance of the two fluxes. Cross helicity values are low within the ICME, but the balance is tipped towards the antisunward direction throughout the ICME volume on average.

While the cross helicity magnitude is low, the balance is tipped towards the antisunward direction – i.e. σ_c^* is positive – on average throughout the flux rope volume. Within the closed-loop framework described above, this could arise, for example, if balance does not typically extend along the full length of the flux rope loop at 1 au and is limited to some region centred on the loop apex. Thus, random spatial sampling of flux rope loops with balanced fluctuations near the apex and more imbalanced, antisunward fluctuations towards the legs would give a positive mean value of σ_c^* overall. Fig. 6 shows a schematic picture of an ICME with lower $|\sigma_c|$ around the rope apex and higher $|\sigma_c|$ in the rope legs connecting back to the Sun. The figure also shows higher $|\sigma_c|$ at higher p (i.e. at larger crossing distances from the rope axis), consistent with Fig. 4. Further analysis would be required to confirm whether ICME legs indeed have the higher $|\sigma_c|$ depicted in Fig. 6.

The extent to which counterpropagating fluctuations reach a balanced state would be dependent on a number of factors, including the time the flux rope spends in the corona during launch, the local Alfvén speed, and field line lengths. Global balance would most easily be achieved near the Sun, where field lines are shorter and the Alfvén speed is higher. The same factors are relevant when considering the large-scale incoherence of ICME structure: Owens (2020) finds that ICMEs are generally too large and expanding too rapidly at 1 au for information propagating at the Alfvén speed to travel from one longitudinal or latitudinal extremity of an ICME to the other.

A further complexity arises if we consider individual flux ropes as tubes that contain twisted field lines with varying lengths. For example, the widely used Lundquist flux rope model has longer, highly twisted field lines in the rope's outer layers and shorter, less twisted field lines running through the core. Therefore, if field line length is a significant factor, longer field lines near the leading and trailing edges might be expected to have less balanced fluctuations in a Lundquist rope. Balance would be further reduced by Alfvén speeds tending to be lower near the rope edges, at least in magnetic clouds (Owens 2020). Cross helicity magnitudes are indeed relatively high towards the trailing edge (Fig. 3), but not at the leading edge. In contrast, Good et al. (2020) found higher $|\sigma_c|$ near both edges within a single magnetic cloud observed at 0.25 au; local interactions with the solar wind and opening of field lines by reconnection (further discussed below) were suggested in that work as potential causes of the higher cross helicity at the rope edges. Note that other rope models (e.g. Gold-Hoyle) have more uniform field line lengths and twists, and such ropes would be expected to have more uniform cross helicity across their radial profiles.

4.2 Interplanetary interactions

Another source of the increasingly more imbalanced, solar wind-like values of cross helicity towards the flux rope rear seen in Figs 3 and 4 could be the erosion described by Dasso et al. (2006), whereby magnetic reconnection progressively peels away the outer field lines of the flux rope, often at the leading edge. In this scenario, the field lines remaining at the trailing edge, which were previously connected to the now-eroded leading edge field, form a connection to the open solar wind field and thus (along with the entrained plasma) acquire more solar wind-like properties. This process potentially occurs from the flux rope launch time onwards. Telloni et al. (2020) recently reported how such erosion could explain significant changes in the large-scale MHD structure of an ICME flux rope observed by aligned spacecraft at 1 and 5.4 au, with the reconnection in this case occurring with a second, trailing ICME.

Cross helicity in ICME sheaths at 1 au is likewise lower than in the solar wind on average, but not as low as in the flux ropes. Since sheaths at 1 au consist of solar wind that has gradually accumulated with ICME propagation in interplanetary space, an interplanetary origin of their reduced cross helicity (e.g. velocity shear) is perhaps more likely. While at low $|\sigma_c|$, antisunward fluctuations still predominate in sheaths: this is consistent with an admixture of pre-existing antisunward fluctuations swept up from the solar wind and a balanced, locally generated population that acts to reduce the overall $|\sigma_c|$. The same effect has been identified in fast–slow solar wind stream interaction regions (SIRs; e.g. Smith et al. 2011), which are in many respects analogous to ICME sheaths.

In the preceding discussion, it has been suggested that the low cross helicity in ICME flux ropes is an intrinsic property that originates in the corona, with the rising σ_c^* through the flux rope profile being due to the effects of reconnection or variable field line lengths. An alternative interpretation is that the entire sheath–ICME complex behaves like an SIR, with the low cross helicity primarily arising in interplanetary space via the ICME–solar wind interaction. Some evidence that supports this hypothesis is found in the bottom two panels of Fig. 4. Taking the presence of shocks as an indicator of stronger ICME–solar wind interaction, it can be seen that ICME flux ropes driving shocks have enhanced levels of $E_\pm^*$ and lower σ_c^* relative to ropes that do not drive shocks. A possible interpretation of Figs 3 and 4 is that $E_\pm^*$ are both amplified at the sheath leading edge and then decay back to ambient solar wind levels (e.g. Pitňa et al. 2017) with distance behind the leading edge. Since the ambient E_-^* is lower than the ambient E_+^*, this could explain why the drop in E_-^* through the ICME is more pronounced. However, it is not clear what physical mechanism could produce such behaviour. The shock (or sheath leading-edge wave, in the case of sheaths without shocks) cannot be the direct cause of the low cross helicity within

the flux rope, since the plasma in the flux rope has not at any stage passed through the shock. Likewise, velocity shears are unlikely to be a cause, since they occur very infrequently or weakly within ICME plasma (Borovsky et al. 2019). However, velocity shear may be the cause of the $E_\pm^*$ enhancement centred at the sheath–flux rope interface.

Coronal and interplanetary modelling would be required to test the range of hypotheses discussed in this section. Besides modelling, additional measurements of ICME cross helicity closer to the Sun would bring some clarity. PSP and *Solar Orbiter* (Müller et al. 2020) are now regularly observing ICMEs in the inner heliosphere (e.g. Davies et al. 2021; Palmerio et al. 2021; Weiss et al. 2021; Möstl et al. 2022). As the number of ICMEs observed by these spacecraft continues to grow, a statistical analysis of ICMEs similar to the one presented here will be possible for sub-1 au heliocentric distances.

5 CONCLUSION

In this study, low cross helicity of fluctuations at inertial range scales has been identified as a typical property of ICME plasma at 1 au. Low cross helicity is indicative of a balance between Alfvénic fluxes propagating parallel and antiparallel to the background magnetic field. The low cross helicity in ICMEs is evident from average values across intervals (Section 3.2) and from superposed epoch analyses (Section 3.3), the latter revealing a systematic variation through the flux rope and sheath sub-structures: the sheath–flux rope complex represents a local depression in cross helicity embedded in the solar wind flow. We suggest that low cross helicity should be considered in the same light as more established interplanetary signatures of ICMEs (Zurbuchen & Richardson 2006). The relatively low cross helicity in ICME flux ropes may primarily originate from their closed field structure, in contrast to the higher cross helicities and more open field structure of the solar wind.

ACKNOWLEDGEMENTS

DATA AVAILABILITY

Data were obtained from the publicly accessible CDAWeb archive at https://cdaweb.sci.gsfc.nasa.gov. The ICME catalogue used in this study is found at https://wind.nasa.gov/ICMEindex.php.

REFERENCES

Al-Haddad N. et al., 2013, Sol. Phys., 284, 129
Ala-Lahti M., Ruohotie J., Good S., Kilpua E. K. J., Lugaz N., 2020, J. Geophys. Res., 125, e28002
Bavassano B., Pietropaolo E., Bruno R., 2000, J. Geophys. Res., 105, 15959
Belcher J. W., Davis Leverett J., 1971, J. Geophys. Res., 76, 3534
Borovsky J. E., 2010, J. Geophys. Res., 115, A09101
Borovsky J. E., 2012, J. Geophys. Res., 117, A05104
Borovsky J. E., Denton M. H., Smith C. W., 2019, J. Geophys. Res., 124, 2406
Bothmer V., Schwenn R., 1998, Ann. Geophys., 16, 1
Bowen T. A., Badman S., Hellinger P., Bale S. D., 2018, ApJ, 854, L33
Burlaga L. F. E., 1991, Magnetic Clouds. Springer-Verlag, Berlin, Heidelberg, New York, p. 152
Cane H. V., Richardson I. G., 2003, J. Geophys. Res., 108, 1156
Chandran B. D. G., Dennis T. J., Quataert E., Bale S. D., 2011, ApJ, 743, 197
Chen C. H. K., 2016, J. Plasma Phys., 82, 535820602
Chen C. H. K., Bale S. D., Salem C. S., Maruca B. A., 2013, ApJ, 770, 125
Dasso S., Mandrini C. H., Démoulin P., Luoni M. L., 2006, A&A, 455, 349
Davies E. E. et al., 2021, A&A, 656, A2
Fox N. J. et al., 2016, Space Sci. Rev., 204, 7
Good S. W., Kilpua E. K. J., Ala-Lahti M., Osmane A., Bale S. D., Zhao L. L., 2020, ApJ, 900, L32
Hamilton K., Smith C. W., Vasquez B. J., Leamon R. J., 2008, J. Geophys. Res., 113, A01106
Kilpua E., Koskinen H. E. J., Pulkkinen T. I., 2017a, Living Rev. Sol. Phys., 14, 5
Kilpua E. K. J., Balogh A., von Steiger R., Liu Y. D., 2017b, Space Sci. Rev., 212, 1271
Kilpua E. K. J. et al., 2019, Space Weather, 17, 1257
Kilpua E. K. J., Good S. W., Ala-Lahti M., Osmane A., Fontaine D., Hadid L., Janvier M., Yordanova E., 2021, Front. Astron. Space Sci., 7, 109
Kiyani K. H., Osman K. T., Chapman S. C., 2015, Phil. Trans. R. Soc. A, 373, 20140155
Leamon R. J., Smith C. W., Ness N. F., 1998, Geophys. Res. Lett., 25, 2505
Lepping R. P. et al., 1995, Space Sci. Rev., 71, 207
Lin R. P. et al., 1995, Space Sci. Rev., 71, 125
Liu Y., Richardson J. D., Belcher J. W., Kasper J. C., Elliott H. A., 2006, J. Geophys. Res., 111, A01102
Lugaz N., Farrugia C. J., Winslow R. M., Al-Haddad N., Kilpua E. K. J., Riley P., 2016, J. Geophys. Res., 121, 10861
Luttrell A. H., Richter A. K., 1987, in Pizzo V. J., Holzer T., Sime D. G., eds, Proceedings of the 6th International Solar Wind Conference, Vol. 2, Solar Wind Six. University Corporation for Atmospheric Research, Boulder, Colorado, p. 335
Lynch B. J., Zurbuchen T. H., Fisk L. A., Antiochos S. K., 2003, J. Geophys. Res., 108, 1239
Marsch E., Tu C. Y., 1990, J. Geophys. Res., 95, 8211
Masías-Meza J. J., Dasso S., Démoulin P., Rodriguez L., Janvier M., 2016, A&A, 592, A118
Möstl C. et al., 2022, ApJ, 924, L6
Müller D. et al., 2020, A&A, 642, A1
Mulligan T., Russell C. T., Luhmann J. G., 1998, Geophys. Res. Lett., 25, 2959
Nieves-Chinchilla T., Linton M. G., Hidalgo M. A., Vourlidas A., Savani N. P., Szabo A., Farrugia C., Yu W., 2016, ApJ, 823, 27
Nieves-Chinchilla T., Vourlidas A., Raymond J. C., Linton M. G., Al-haddad N., Savani N. P., Szabo A., Hidalgo M. A., 2018, Sol. Phys., 293, 25
Nieves-Chinchilla T., Jian L. K., Balmaceda L., Vourlidas A., dos Santos L. F. G., Szabo A., 2019, Sol. Phys., 294, 89
Owens M. J., 2020, Sol. Phys., 295, 148
Palmerio E., Kay C., Al-Haddad N., Lynch B. J., Yu W., Stevens M. L., Pal S., Lee C. O., 2021, ApJ, 920, 65
Perez J. C., Boldyrev S., 2009, Phys. Rev. Lett., 102, 025003
Pitňa A., Šafránková J., Němeček Z., Franci L., 2017, ApJ, 844, 51
Riley P. et al., 2004, J. Atmos. Sol.-Terr. Phys., 66, 1321
Rodriguez L. et al., 2016, Sol. Phys., 291, 2145
Salman T. M., Lugaz N., Farrugia C. J., Winslow R. M., Jian L. K., Galvin A. B., 2020, ApJ, 904, 177
Schekochihin A. A., 2020, preprint (arXiv:2010.00699)
Smith C. W., Tessein J. A., Vasquez B. J., Skoug R. M., 2011, J. Geophys. Res., 116, A10103

Sorriso-Valvo L., Yordanova E., Dimmock A. P., Telloni D., 2021, ApJ, 919, L30

Stansby D., Horbury T. S., Matteini L., 2019, MNRAS, 482, 1706

Telloni D. et al., 2020, ApJ, 905, L12

Torrence C., Compo G. P., 1998, Bull. Am. Meteorolog. Soc., 79, 61

Tsurutani B. T., Gonzalez W. D., Tang F., Akasofu S. I., Smith E. J., 1988, J. Geophys. Res., 93, 8519

Weiss A. J. et al., 2021, A&A, 656, A13

Wilson R. M., 1987, Planet. Space Sci., 35, 329

Zhang G., Burlaga L. F., 1988, J. Geophys. Res., 93, 2511

Zurbuchen T. H., Richardson I. G., 2006, Space Sci. Rev., 123, 31

This paper has been typeset from a T_EX/L^AT_EX file prepared by the author.